



# Spatiotemporal characterization of nonlinear intermodal interference between selectively excited modes of a few-mode fiber

**SAI KANTH DACHA<sup>1,2,\*</sup>** AND **THOMAS E. MURPHY<sup>1,3</sup>**

<sup>1</sup>*Institute for Research in Electronics and Applied Physics, University of Maryland, College Park, Maryland 20740, USA*

<sup>2</sup>*Department of Physics, University of Maryland, College Park, Maryland 20740, USA*

<sup>3</sup>*Department of Electrical and Computer Engineering, University of Maryland, College Park, Maryland 20740, USA*

\*Corresponding author: [sdacha@umd.edu](mailto:sdacha@umd.edu)

Received 2 September 2020; revised 10 November 2020; accepted 11 November 2020 (Doc. ID 409060); published 17 December 2020

Nonlinear propagation of signals in single-mode fibers is well understood, and is typically observed by measuring the temporal profile or optical spectrum of an emerging signal. In multimode fibers, the nonlinearity has both a spatial and a temporal element, and a complete investigation of the interactions between propagating modes requires resolving the output in both space and time. We report here spatiotemporal measurements of a time-dependent mode interference effect, arising from the Kerr nonlinearity, of two selectively excited  $LP_{0m}$  modes of a step-index few-mode fiber. We describe a method to selectively excite two propagating modes through the use of a phase mask directly patterned on the entrance face of the fiber. The output is resolved by raster-scanning a near-field tapered single-mode optical fiber probe that is connected to a high-speed detector. The results show that in the presence of nonlinearity, the output exhibits a spatiotemporal character that cannot be adequately characterized by a camera image or pulse shape alone. © 2020 Optical Society of America under the terms of the [OSA Open Access Publishing Agreement](#)

<https://doi.org/10.1364/OPTICA.409060>

## 1. INTRODUCTION

The rapid growth in demand for long-haul fiber-optic communication systems has fueled an interest in understanding nonlinear optics in fibers, as nonlinear impairments are now understood to be a critical feature that limits the transmission capacity of optical networks [1,2]. In the face of ever-increasing bandwidth demand, spatial division multiplexing (SDM) has emerged as a new frontier to improve network capacity [3]. Although multimode fibers (MMFs) pre-date single-mode fibers, nonlinear effects in MMFs have received comparatively little attention, because until recently MMFs had been primarily relegated to short-distance, low-power links. As few-mode fibers (FMFs) and MMFs become more prevalent in longer-distance networks, and with the advent of techniques for spatially multiplexed optical amplification [4], nonlinear effects are expected to play an increasingly important role [5].

Multimode nonlinear optics is inherently more complex than single-mode nonlinear optics because of the spatial degree of freedom. Commercially available MMFs support a large number ( $\sim 100$  s) of transverse spatial modes, which gives rise to a variety of intramodal and intermodal nonlinear interactions. A plethora of spatiotemporal nonlinear phenomena have been uncovered in recent experiments, including Kerr-induced beam cleanup [6,7], multimode solitons [8], geometric parametric instability [9], multi-octave spanning supercontinuum generation [10], and spatiotemporal modulation instability [11]. Such phenomena are

of great interest not only from a fundamental science perspective, but also in practical applications ranging from high-power beam delivery and high-power fiber lasers to supercontinuum light sources and optical metrology [12].

Here, we seek to address two key shortcomings in the way multimode nonlinearity is measured and modeled. The first relates to experimental measurement techniques. Traditional measurement techniques, including spectral and temporal measurements of the entire beam and spatial imaging using cameras, average over two out of the three measurement axes (space, time, and spectrum). In the most common type of measurements (spectral measurements coupled with spatial imaging of the output), both the spectrum analyzer as well as the CCD/CMOS camera average over many pulses. As a result, many interesting dynamics that happen within one pulse duration are missed, and the spatiotemporal nature of multimode nonlinearity is not captured. We address this problem by introducing a method for measuring the output MMFs and FMFs in both space and time. Specifically, we raster-scan a near-field scanning optical microscope (NSOM) tip in the near field of the MMF/FMF output end-face, while collecting a time trace at each spatial location. By stitching together the measured spatially resolved time traces, we demonstrate the temporal evolution of the instantaneous intensity profile within one optical pulse. Here, we report a complete spatiotemporal measurement of the entire

output beam, measured directly in the near field with a spatial resolution of 400 nm.

Spatiotemporal and spatirospectral measurements of optical beams, modes, and pulses is relevant in many areas in optics, and several techniques have been developed to resolve a light beam in space and time/spectrum simultaneously. Nicholson *et al.* report spatially and spectrally resolved imaging, wherein spatially resolved power spectral measurements are performed to characterize the modal content of large-mode-area (LMA) MMFs [13]. Such a technique is ideally suited for studying the nonlinear propagation of short (femtosecond to picosecond) pulses in MMFs/FMFs. Other techniques yield more information about the pulse, including the phase of the electric field, and are also better suited for short pulses (femtosecond to picosecond) [14–17]. Such techniques, however, typically require interference with a reference beam, thereby requiring careful alignment, as well as post-processing of experimental data and are not direct measurements. In the broader context of existing methods for spatiotemporal pulse characterization, the technique that we introduce here is ideal for directly measuring the spatiotemporal intensity of multimoded long pulses (nanosecond) with a spatial resolution exceeding the diffraction limit.

There is growing recognition, backed by experimental measurements, that the nonlinearity in MMFs is spatiotemporal in nature. In [18], Krupa *et al.* used a small-area high-speed photodetector to measure different temporal pulse profiles at different positions in the collimated output beam from a graded-index MMF. In [19], Krupa *et al.* used a small-area high-speed photodetector to measure the temporal pulse profile at different positions in the collimated output beam from a graded-index MMF to study supercontinuum generation. In [20], Jing *et al.* employed spatiotemporal-spectral compressed ultrafast photography to image dissipative solitons in MMFs. More recently, a measurement technique similar to the one presented here has been independently proposed, where a single-mode fiber is scanned across the magnified output beam of a graded-index MMF to demonstrate the spatiotemporal nature of Kerr-induced beam clean-up [21,22]. The spatial resolution of measurement techniques involving beam magnification, however, is limited by diffraction, and the near-field measurement technique presented here is capable of offering a much higher spatial resolution that could be especially useful for studying smaller-core-area FMFs.

The second shortcoming we seek to address here relates to the modeling of multimode nonlinearity. Currently, there exist two complementary models of nonlinear propagation of optical pulses in MMFs: the (3 + 1)D nonlinear Schrödinger partial differential equation for the complex field envelope (also known as the Gross-Pitaevskii equation), and the generalized multimode nonlinear Schrödinger equations (GMM-NLSE) [23]. The nonlinear wave equation is most efficient for numerically simulating the nonlinear propagation of pulses when a large ( $\sim 100$  s) number of modes are excited [9], while the GMM-NLSE is best suited for studying and numerically simulating propagation when the number of excited modes is small ( $\sim 10$  s). The GMM-NLSE treats optical nonlinearity as acting at the modal level. The validity of the latter picture of nonlinearity is of fundamental importance not only in establishing a more complete understanding of multimode nonlinear effects broadly, but also specifically in FMF-based SDM applications where the number of co-propagating modes is small. To study this problem, we choose a step-index FMF, and we further restrict the

already small number of allowed modes in FMFs by etching a phase mask directly on the FMF input end-face by means of focused ion-beam (FIB) milling. The phase mask restricts the number of excited modes to the smallest non-trivial number possible: two. Upon measuring the output of this system in space and time simultaneously, we report the observation of a time-dependent interference effect of the two propagating modes that is distinctly spatiotemporal as well as nonlinear in nature. We then compare our results with the predictions of the GMM-NLSE and its modal treatment of nonlinearity.

## 2. SELECTIVE MODE EXCITATION

Under the weakly guiding approximation, a linearly polarized (LP) optical signal with carrier frequency  $\omega$  traveling in a few-mode optical fiber can be represented as

$$\mathbf{E}(r, \phi, z, t) = \hat{\mathbf{x}} \sum_p A_p(z, t) \psi_p(r, \phi) e^{i(\beta_p z - \omega t)}, \quad (1)$$

where  $\psi_p(r, \phi)$  represents an LP mode of the fiber, with corresponding propagation constant  $\beta_p$ , and  $A_p(z, t)$  is the slowly varying complex envelope. To simplify the notation, here, we contract the azimuthal and radial indices ( $l, m$ ) into a single index  $p$  that enumerates the LP modes.

For the experimental conditions considered here, we selectively excite only the radially symmetric ( $LP_{0m}$ ) modes, which are given by

$$\begin{aligned} \psi_p(r) = N_p & \begin{cases} J_0(U_p r/a), & r \leq a \\ K_0(W_p r/a), & r > a \end{cases}, \quad U_p \equiv a \sqrt{\frac{n_1^2 \omega^2}{c^2} - \beta_p^2}, \\ W_p & \equiv a \sqrt{\beta_p^2 - \frac{n_2^2 \omega^2}{c^2}}. \end{aligned} \quad (2)$$

The propagation constants  $\beta_p$  and related values  $U_p$  and  $W_p$  are determined by requiring that  $\psi_p(r)$  and  $\psi'_p(r)$  are continuous at the boundary  $r = a$ , and the normalization constant  $N_p$  is chosen so that  $|A_p(z, t)|^2$  represents the instantaneous power carried by the  $p$ th mode.

The step-index FMF considered in this work has a core diameter  $2a = 20 \mu\text{m}$  and numerical aperture of 0.14. At our laser wavelength  $\lambda = 1064 \text{ nm}$ , this fiber supports 17 LP modes, of which three are radially symmetric:  $LP_{01}$ ,  $LP_{02}$ , and  $LP_{03}$ , which we label  $p = 1, 2$ , and 3, respectively.

If the input face of the optical fiber is illuminated by a symmetrical, focused, linearly polarized, Gaussian optical beam described by  $\Phi(r) = \exp(-r^2/w^2)$ , then a superposition of the radially symmetric modes will be excited, and the relative portion of power coupled into each of these modes is

$$\eta_p \equiv \frac{|A_p(z=0, t)|^2}{P_0(t)} = \frac{|\int \Phi(r) \psi_p(r) dA|^2}{\int |\Phi^2(r)| dA \int |\psi_p^2(r)| dA}, \quad (3)$$

where  $P_0(t)$  represents the total power of the incident Gaussian beam.

In Fig. 1, we plot the numerically calculated modal coupling efficiencies  $\eta_p$  for the three radially symmetric modes as a function

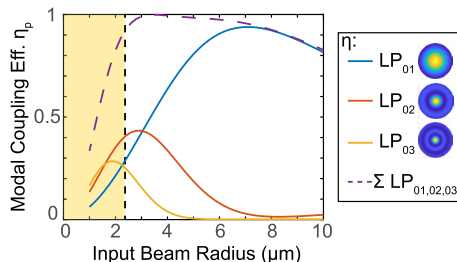


**Fig. 1.** Modal coupling efficiencies versus input beam radius. For beam radii to the left of the dashed vertical line, the overall coupling efficiency of light into the FMF falls off quickly. To maintain good overall coupling efficiency, input beam radius must be larger than  $2.3\ \mu\text{m}$ .

of input beam radius  $w$ , along with the total coupled power efficiency,  $\eta_1 + \eta_2 + \eta_3$ . The total coupled optical power decreases well below unity for input excitations smaller than  $w = 2\ \mu\text{m}$ , because in this regime, the focused Gaussian beam exceeds the numerical aperture of the fiber. From Fig. 1, one concludes that with a simple Gaussian beam, it is not possible to excite one higher-order mode exclusively, and more importantly, it is not possible to selectively excite a combination of two modes with comparable powers without also launching significant power in the third mode. To best isolate and study the nonlinear interaction between propagating modes, we seek a method for selectively, efficiently, and exclusively exciting a pair of modes, which is impossible with a simple Gaussian input beam.

Selective excitation of spatial modes has been previously achieved using spatial light modulators (SLMs) [24,25] together with projection optics. However, spatial modulators can be bulky and difficult to align, and are prone to damage under the high fluence illumination required to observe nonlinear optical effects. Selective excitation of orbital angular momentum (OAM) modes has also been achieved using forked diffraction gratings patterned directly on the fiber end-face [26], but the diffraction efficiency can significantly limit the coupled optical power, which again hinders the observation of nonlinear optical effects. Here, we employ a new method of directly imparting a binary phase pattern onto the incident Gaussian beam by modifying the fiber end-face. Our method is inspired by the thin-film deposition reported by Chen *et al.* [27], but instead of depositing and patterning thin films onto the input end-face, we directly etch a phase mask onto the input end-face of the FMF using FIB milling.

Although SLMs allow for more flexibility, a phase mask directly written onto the end-face of the fiber has significant advantages: it is lighter, more robust, more compact, and has no need for relay optics or alignment. It is also better suited for high-power nonlinear optical applications and could be useful in spatially multiplexed amplification schemes for future SDM systems. Phase masks on fiber end-faces also find use in applications such as miniaturization of optical elements, beam shaping for medical devices, generation of OAM light, and particle trapping [28–31].

Patterning the end-face of an optical fiber has been achieved using a variety of techniques such as photolithography, nanoimprinting, e-beam lithography, two-photon polymerization, FIB milling and thin-film deposition [32]. Here, we opt for FIB, as it is a powerful and convenient prototyping tool, and does not require the use of a photo-resist. Any of the other aforementioned lithographic techniques can be employed to reproduce phase patterns similar to the one described here.

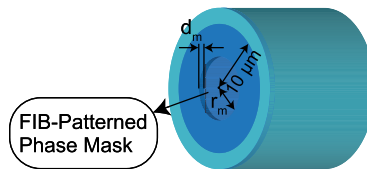


**Fig. 2.** Graphical illustration of an FIB-patterned phase mask on the input end-face of the FMF. The highlighted region at the center of the core represents the region where  $\text{SiO}_2$  was removed in the milling process (cladding diameter not to scale).

Although FIB milling permits nearly arbitrary spatial structures, we have found that a simple binary radial pattern provides sufficient degrees of freedom to selectively and efficiently excite two radial modes. Prior to fabrication, the FMF end-face is coated with a 100 nm layer of Au:Pd alloy to make the sample conducting to help mitigate charging effects during the milling process. An accelerated beam of  $\text{Ga}^+$  ions is focused onto the FMF input end-face to a spot size of 90 nm and raster-scanned to remove a centered disc pattern of radius  $r_m$  and depth  $d_m$ , as shown in Fig. 2. Because the core-cladding boundary is not discernable on the end-face through electron microscopy, the focused ion beam write-pattern was aligned to the fiber outer diameter. The removal of  $\text{SiO}_2$  in the disc region imparts a phase difference  $\Theta(r)$  to the near-field coupled light, thereby creating a spatial phase mask described by

$$\Theta(r) = \begin{cases} (n_1 - 1) \frac{\omega}{c} d_m, & r \leq r_m \\ 0, & r > r_m \end{cases}. \quad (4)$$

In the presence of a phase mask described by the function  $\Theta(r)$ , the launched modal coupling efficiencies are re-calculated to be

$$\eta_p = \frac{\left| \int \Phi(r) e^{i\Theta(r)} \psi_p(r) dA \right|^2}{\int |\Phi^2(r)| dA \int |\psi_p^2(r)| dA}, \quad (5)$$

where, as before,  $\Phi(r) = \exp(-r^2/w^2)$ . Figure 3 shows the calculated coupling efficiency for the three radial modes, as a function of the two degrees of freedom ( $d_m, r_m$ ), for a fixed input beam radius of  $w = 8.4\ \mu\text{m}$ . The radius of the mask is varied from 0 to  $10\ \mu\text{m}$ , while the depth of mask is varied from 0 to  $1\ \mu\text{m}$  (approximately one wavelength). Regions of interest on this color map include those that have negligible power in one mode and comparable power in the other two. The chosen operating point is marked by \* (in green) in Fig. 3, at which the  $\text{LP}_{03}$  color map shows very low coupling efficiency, while  $\text{LP}_{01}$  and  $\text{LP}_{02}$  color maps show comparable efficiencies. The calculated modal coupling efficiencies at this point are  $\eta_1 = 0.47$ ,  $\eta_2 = 0.31$ , and  $\eta_3 < 0.01$  for  $\text{LP}_{01}$ ,  $\text{LP}_{02}$ , and  $\text{LP}_{03}$  modes, respectively. The final result of this FIB milling

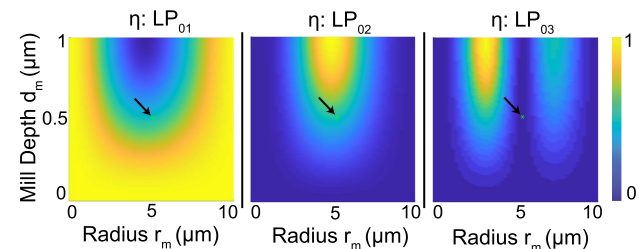


**Fig. 3.** Numerical calculation of modal coupling efficiencies as a function of phase mask radius ( $r_m$ ) and depth ( $d_m$ ). The chosen operating point marked by \* in green is  $(r_m^*, d_m^*) = (5.28\ \mu\text{m}, 0.53\ \mu\text{m})$ .

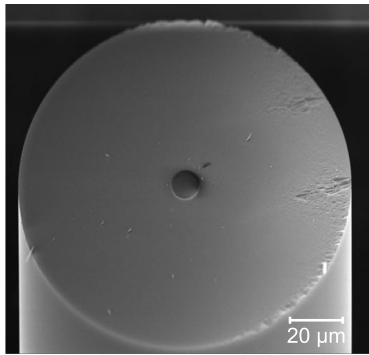


**Fig. 4.** Scanning electron micrograph (SEM) of FMF input end-face after FIB milling process. The darker disc at the center indicates the area where milling was performed.

process is shown in the scanning electron microscopy (SEM) image of the FMF input end-face shown in Fig. 4.

### 3. THEORY AND MODELING OF NONLINEAR PROPAGATION

In single-mode fibers, pulse propagation in the presence of optical Kerr nonlinearity is described by the NLSE. In MMFs and FMFs, the single equation must be replaced by the GMM-NLSE—a set of coupled partial differential equations that govern the evolution and mixing of the mode amplitudes [23]. The equation governing the  $p$ th mode amplitude is

$$\frac{\partial A_p}{\partial z} = -\beta'_p \frac{\partial A_p}{\partial t} - i \frac{\beta''_p}{2} \frac{\partial^2 A_p}{\partial t^2} + i \sum_{l,m,n} \gamma_{lmnp} A_l A_m A_n^* e^{i \Delta \beta_{lmnp} z}, \quad (6)$$

where  $\beta'_p$  and  $\beta''_p$  are the first- and second-order Taylor series coefficients of the propagation constant  $\beta_p(\omega)$  about the optical carrier frequency  $\omega$ , which relate to the group velocity and chromatic dispersion, respectively. The phase mismatch is given by

$$\Delta \beta_{lmnp} \equiv \beta_l + \beta_m - \beta_n - \beta_p, \quad (7)$$

and the nonlinear coefficient governing the mixing between modes is

$$\gamma_{lmnp} \equiv \frac{n_2 \omega}{c A_{lmnp}}, \quad (8)$$

where  $n_2$  is the nonlinear refractive index, and  $A_{lmnp}$  is an effective area:

$$A_{lmnp} \equiv \frac{\sqrt{\int |\psi_l|^2 dA \int |\psi_m|^2 dA \int |\psi_n|^2 dA \int |\psi_p|^2 dA}}{\int \psi_l^* \psi_m \psi_n^* \psi_p dA}. \quad (9)$$

Earlier treatments of this problem [23] assumed a common  $z$  dependence of  $e^{i \beta_0 z}$  for all modes in (1), which eliminates the phase mismatch  $\Delta \beta_{lmnp}$ , but instead introduces an additional term  $i(\beta_p - \beta_0)A_p$  on the right-hand-side of (6). The equivalent formulation presented here is more convenient and easier to numerically integrate for lower-peak-power quasi-CW optical pulses. For the pulse duration and fiber length considered here, the chromatic dispersion term can be safely ignored ( $\beta''_p = 0$ ), and we can further ignore the differential group delay between the interacting modes, i.e., we assume that  $\beta'_p$  are all equal. We can also assume that the random linear mode coupling is negligible. The fiber length over which random linear mode coupling is

negligible depends upon the spatial homogeneity of the fiber and the mode spacing [33]. Prior experiments on MMFs observe that an effective index separation  $\Delta n_{\text{eff}} \geq 10^{-4}$  between propagating modes results in negligible linear mode mixing over 10–100 m of propagation [34,35]. In our experiment, the length of the fiber is only 1.24 m, and the excited modes are separated in an effective index from all other modes of the fiber by  $\Delta n_{\text{eff}} > 3 \times 10^{-4}$ .

For the FMF under consideration, there are 17 modes per polarization state at  $\lambda = 1064$  nm, and therefore, (6) represents a set of 17 coupled nonlinear equations, with up to  $17^4 = 83,521$  nonlinear coupling coefficients  $\gamma_{lmnp}$  and phase mismatch terms  $\Delta \beta_{lmnp}$ . Fortunately, many of the terms can be neglected due to vanishing nonlinear coefficients and/or non-vanishing phase mismatch  $\Delta \beta_{lmnp}$ . Of the  $17^4$  possible combinations of  $\{lmnp\}$ , only 1807 terms (about 2%) have vanishing  $\Delta \beta_{lmnp}$  (i.e., are phase matched). The smallest nonzero  $\Delta \beta_{lmnp}$  is  $9.15 \text{ m}^{-1}$ , which is large compared to  $1/L$  (where  $L$  is the fiber length considered in our experiment). As a result, all of the terms with non-vanishing  $\Delta \beta_{lmnp}$  average to zero over the length of the fiber [36]. Of the 1807 terms with vanishing  $\Delta \beta_{lmnp}$ , 1200 also have a vanishing  $\gamma_{lmnp}$  because of symmetry. This leaves only 607 of the  $17^4$  total possible nonlinear terms remaining in the NLSEs. For the radially symmetric modes, only the self- and cross-phase modulation terms remain, and it is easy to prove that the modal power is conserved during propagation (i.e.,  $d|A_1^2|/dz = d|A_2^2|/dz = 0$ ). Because we selectively excite only these two modes at the input of the fiber, as described in Section 2, we can safely ignore the cross-phase modulation terms from all higher-order modes. As a result, the coupled NLSEs simplify to

$$\frac{\partial A_1}{\partial z} + \beta' \frac{\partial A_1}{\partial t} = i (\gamma_{1111} |A_1|^2 + 2\gamma_{1212} |A_2|^2) A_1, \quad (10)$$

$$\frac{\partial A_2}{\partial z} + \beta' \frac{\partial A_2}{\partial t} = i (\gamma_{2222} |A_1|^2 + 2\gamma_{1212} |A_1|^2) A_2, \quad (11)$$

where the coefficients  $\gamma_{1111}$  and  $\gamma_{2222}$  describe self-phase modulation, and  $\gamma_{1212}$  describes cross-phase modulation between the two excited modes. These equations can be directly integrated, to yield

$$A_1(L, \tau) = A_1(0, \tau) \exp [i(\gamma_{1111} |A_1|^2 + 2\gamma_{1212} |A_2|^2) L], \quad (12)$$

$$A_2(L, \tau) = A_2(0, \tau) \exp [i(\gamma_{2222} |A_2|^2 + 2\gamma_{1212} |A_1|^2) L], \quad (13)$$

where  $\tau \equiv t - \beta' L$  is the retarded time. The spatial intensity emerging at the end of the fiber is given by

$$I(r, z=L, t) = \frac{1}{2} n \epsilon_0 c |\mathbf{E}(r, z=L, t)|^2 \quad (14)$$

$$= \frac{1}{2} n \epsilon_0 c |\psi_1(r) A_1(L, \tau) e^{i \beta_1 L} + \psi_2(r) A_2(L, \tau) e^{i \beta_2 L}|^2 \quad (15)$$

$$= \frac{1}{2} n \epsilon_0 c P(\tau) [\eta_1 \psi_1^2(r) + 2\sqrt{\eta_1 \eta_2} \psi_1(r) \psi_2(r) \cos(\Delta\phi) + \eta_2 \psi_2^2(r)], \quad (16)$$

where  $P(\tau)$  describes the optical pulse shape time,  $\eta_1$  and  $\eta_2$  denote the power excitation efficiencies of the LP<sub>01</sub> and LP<sub>02</sub> modes, respectively, and  $\Delta\phi$  is the power-dependent relative phase shift between the two modes emerging from the fiber:

$$\Delta\phi(\tau) = \phi_0 + [\gamma_{2222}\eta_2 + 2\gamma_{1212}(\eta_2 - \eta_1) - \gamma_{1111}\eta_1] P(\tau)L. \quad (17)$$

The phase offset  $\phi_0$  appearing in (17) refers to the unknown relative linear phase of the two modes emerging from the fiber, which depends sensitively on the fiber length and the input relative phase difference. We note, once again, that we have chosen to restrict the number of excited modes in this study to  $n = 2$  so as to simplify the analysis and allow for a direct and quantitative comparison of theory, simulation, and experiment. In the presence of  $n > 2$  modes, the number of cross terms in (16) would scale as  $n(n - 1)/2$ , which is equal to the number of possible mode pairs. Each such cross term would have a unique uncontrolled parameter [similar to  $\phi_0$  in (17)] that depends sensitively on the fiber length and the difference in propagation constants of the mode pair. For  $n = 2$ , we have only one such term, which greatly simplifies comparison of numerical simulation and experimental observations, although the output measurement technique presented in the following section does not depend on the number of excited modes.

Because the transverse modes differ, the degree of interference between them will be spatially dependent. Because the pulse shape  $P(\tau)$  is time dependent, it produces a time-varying nonlinear phase shift between the modes. These effects combine to produce a spatiotemporal nonlinear pattern at the output end-face. If the input pulse is Gaussian in time, it will split into two spatial modes, which each acquire different nonlinear chirps, as the pulse intensity rises and then falls. If the peak nonlinear phase difference approaches or exceeds  $\pi$ , the local intensity emerging from the fiber will exhibit a pattern of temporal interference fringes associated with the turn-on and turn-off of the pulse.

These broad predictions of the analytical model form a starting point with which to compare the results of our numerical simulations and experimental results. In the following sections, we present our experimental setup and measurements, and compare them with the numerical split-step Fourier method (SSFM) simulations of (6).

#### 4. EXPERIMENT

The experimental setup, as shown in Fig. 5, consists of a YAG microchip laser ( $\lambda_0 = 1064$  nm) that produces 720 ps pulses at a 1 kHz repetition rate. The laser pulses have a maximum energy of 135  $\mu$ J, and the energy of the pulses entering the FMF is controlled by a half-wave plate (HWP) and polarizing beam splitter (PBS) such that the input peak power is 15 kW. Using a plano-convex lens of focal length  $f = 25.4$  mm, the laser beam is focused to a spot with radius 8.4  $\mu$ m on the patterned input end-face of a 20  $\mu$ m step-index fiber with numerical aperture NA = 0.14 and length  $L = 1.24$  m. The length of the fiber is restricted to approximately 1 m for two reasons: first, the differential group delay between the two excited modes per unit length of the fiber, given by  $(\beta'_1 - \beta'_2)$ , is on the order of 10 ps/m at our laser wavelength. For the duration of our pulse (720 ps), a fiber length of more than a few meters will cause a significant walk-off between the peaks of the pulses in the two spatial modes. For efficient nonlinear interaction, we desire that the temporal walk-off between the two modes be minimal. Second, as mentioned in Section 3, longer fiber lengths are more prone to random linear mode coupling.

At the output end-face of the FMF, we employ an NSOM tip that is brought in close proximity ( $\ll 1$   $\mu$ m) to the FMF end-face. The NSOM tip has an aperture of  $250 \pm 50$  nm, and tapers into a single-mode fiber segment connected to a 10 GHz photo-receiver

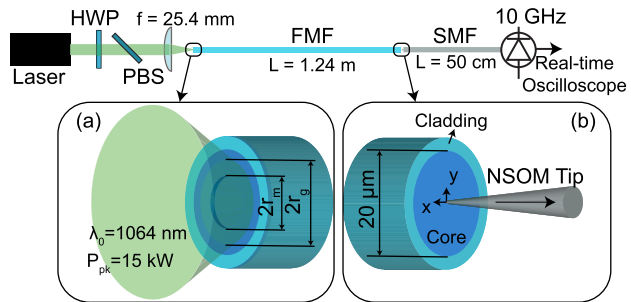


**Fig. 5.** Experimental schematic for performing spatiotemporal measurements of nonlinear interactions between selectively excited spatial modes of an FMF. (a) A Gaussian beam of radius  $r_g = 8.4 \mu\text{m}$  is incident on the patterned FMF input end-face; mask radius  $r_m = 5.28 \mu\text{m}$ . (b) Raster-scanned NSOM fiber tip for recording spatiotemporal measurements at FMF output end-face; the separation between the FMF end-face and NSOM tip is 1  $\mu\text{m}$ .

and recorded using a real-time oscilloscope. The resolution of the temporal measurements is 100 ps, and is limited only by the bandwidth of the photodiode used. The NSOM tip is scanned across the output end-face of the FMF using a two-axis piezo-controlled translation stage. Using this, we record the temporal output along a  $20 \mu\text{m} \times 20 \mu\text{m}$  grid of pixels on the FMF output end-face at a resolution of a 400 nm. We then reconstruct a temporal evolution of the 2D intensity profile exiting the FMF end-face. It must be noted that commercially available NSOM tips can have apertures as small as 50 nm, which can be used to achieve spatial resolution below 100 nm. For comparison, the diffraction-limited resolution achievable using a high-magnification, high-numerical-aperture (NA 0.75) microscope objective lens at  $\lambda = 1064$  nm is given by  $\lambda/2\text{NA} \approx 710$  nm.

To minimize the timing jitter associated with the pulse generation and detection, we reflected 1% of the incident pulse to a second high-speed photodiode, which was used to confirm the pulse energy stability and trigger the oscilloscope.

#### 5. RESULTS AND DISCUSSION

Figure 6(a) shows, for reference, the radial profiles of the two selectively excited modes: LP<sub>01</sub> and LP<sub>02</sub>. Figures 6(b)–6(d) show the time-domain output recorded at three selected spatial locations:  $r = 0$  (on-axis),  $r = 4.4 \mu\text{m}$ , and  $r = 7.2 \mu\text{m}$ , respectively. We observe interference fringes in the time domain arising from the overlap, in time and space, of two modes that have acquired different nonlinear chirps. Further, at the three selected values of  $r$ , the two modes have different field amplitudes, leading to a different time-domain pattern at each position  $r$ .

The temporal data are then used to reconstruct the 2D spatial intensity pattern at the FMF output for time instances within one pulse duration. By stitching together all of the time traces into a mosaic of time-varying pixels, we construct what one would see at the output with a picosecond resolution ultrafast video camera. Figure 7 (Visualization 1 and Visualization 2) shows the output of such a reconstruction at three different times during the pulse.

From (17), in the absence of nonlinearity, the output spatial intensity profile is determined by the linear phase difference  $\phi_0$  acquired by the two modes during propagation. The beat length between the LP<sub>01</sub> and LP<sub>02</sub> modes is approximately  $1/(\beta_1 - \beta_2) = 89 \mu\text{m}$ , and because the fiber length  $L$  cannot

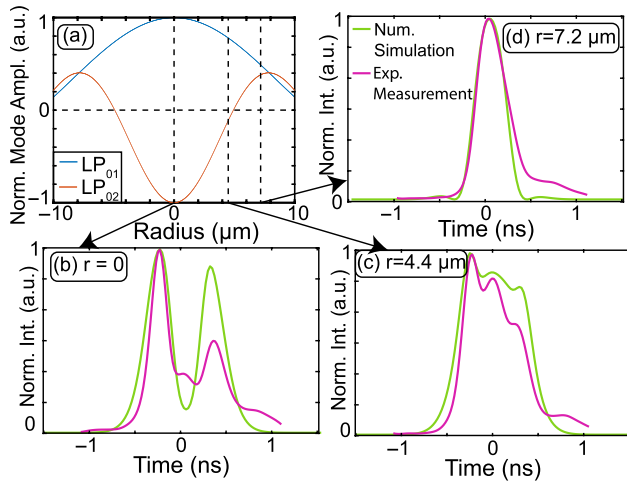


**Fig. 6.** Spatially resolved temporal measurements: (a) radial amplitude profiles of LP<sub>01</sub> and LP<sub>02</sub> modes; (b)–(d) output temporal measurements at  $r = 0$  (on-axis),  $r = 4.4 \mu\text{m}$ , and  $r = 7.2 \mu\text{m}$ . Input pulse peak power is 15 kW.

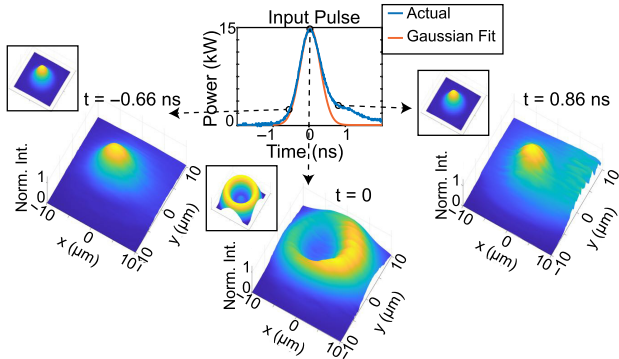


**Fig. 7.** Spatiotemporal reconstruction of output pulse at FMF output end-face. Output 2D spatial intensity profile (reconstructed from experimental data) at three time instances within the pulse:  $t = -0.66 \text{ ns}$ ,  $t = 0$ , and  $t = 0.86 \text{ ns}$  (see Visualization 1). Numerical simulation results are shown in inset boxes (see Visualization 2).

be controlled or measured to this precision, we take the linear phase offset to be an unknown numerical parameter. By fitting the measured output beam shape at low power, we determine  $\phi_0 = 0.58\pi$ .

As the pulse rises to its peak, the nonlinearity can no longer be neglected, and the two modes acquire a time-dependent nonlinear phase difference. Using (17), the peak nonlinear phase difference between the two modes acquire at the pulse peak ( $t = 0$ ) is calculated to be approximately equal to one  $\pi$ , based on the pulse power and estimated modal coupling efficiencies.

This phase difference has two key manifestations. First, as shown in Fig. 7, at  $t = 0$ , the on-axis spatial maximum observed at low power is converted to an on-axis minimum, thereby converting the Gaussian-like beam to an annulus-shaped beam. Second, at the on-axis point, the same destructive interference of the modes causes a local minimum at  $t = 0$ , resulting in the formation of the temporal fringes as shown in Fig. 6(b).

As shown in Fig. 6(a), the LP<sub>02</sub> mode  $\psi_2(r)$  changes sign at  $r = 4.9 \mu\text{m}$ , which spatially alters the interference between the modes: whenever the two modes interfere constructively

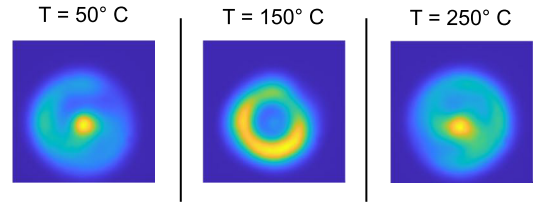


**Fig. 8.** FMF output recorded on a CMOS camera at low input power at three different temperatures. As the temperature of an 18 cm long FMF section is increased, the length of the core increases on the micrometer scale due to thermal expansion, leading to a slightly different modal overlap at each temperature. As the temperature is swept from 50°C to 150°C, the output intensity profile switches between a Gaussian-like shape and an annulus, just as it did within one pulse duration in the presence of nonlinearity.

(add) on-axis, they will interfere destructively (subtract) in the region  $r > 4.9 \mu\text{m}$ , and vice versa. For the time traces collected at  $r = 7.2 \mu\text{m}$  [Fig. 6(d)], we indeed observe a temporal *maximum* at  $t = 0$ , in comparison to the local minimum observed at  $r = 0$  [Fig. 6(b)]. This observation suggests that the nonlinear component of the phase difference remains the same at both spatial locations, which confirms the validity of the modal treatment of nonlinearity.

The green curves in Fig. 6 show the numerically computed output temporal intensity profile, obtained by solving (9), which shows excellent agreement with the experimental measurements. The inset images in Fig. 7 likewise show the numerically calculated spatial patterns at three different times within the pulse. The numerical simulations assume a mode admixture of  $\eta_1 = 0.47$  and  $\eta_2 = 0.31$ , calculated from (5), and a phase offset of  $\phi_0 = 0.58\pi$ , which was separately determined by fitting the beam shape in the low-power limit. Unlike the simplified treatment of (10) and (11), the simulations included a small, calculated differential group delay ( $\beta'_1 \neq \beta'_2$ ), which results in the observed temporal asymmetry in the output pulses.

To further verify that the observed spatiotemporal features result from two-mode interference, we attenuated the laser, and instead used a hot-plate applied to an 18 cm section of fiber, to thermally adjust the linear phase difference  $\phi_0$  between the two modes. Heating of the fiber changes both the refractive indices through the thermo-optic effect and the fiber length via thermal expansion. The latter is believed to be the dominant effect that controls  $\phi_0$ . Figure 8 shows the measured output field patterns, observed using a CCD camera, at three different hot-plate temperatures, which shows the cyclical progression of patterns from axial to annular and back. This pattern is identical to what occurs in time because of self- and cross-phase modulation by the optical Kerr effect during the Gaussian pulse.

The agreement among the predictions of our simplified analytical model, numerical simulations of the complete GMM-NLSE (6), spatiotemporal measurements, as well as thermal measurements indicates the validity of the modal picture of nonlinearity.

## 6. CONCLUSION

To probe the nonlinear interaction between two individual spatial modes, it is desirable to preferentially excite only the modes of interest. We achieved this using a novel implementation of a phase

mask, which involves etching the mask directly onto the fiber input end-face by means of FIB milling. While hard-writing a mask onto the input end-face has the disadvantage of being less flexible as compared to an SLM setup, it has some key advantages such as compactness and ease of integration into chip-scale photonic circuits. Such a mask is also not prone to damage under the influence of high laser power, and is a power-efficient way to excite a desired mode combination. Phase masks etched onto fiber end-faces also have numerous applications in beam shaping and miniaturization of optical devices, and could be useful in spatially multiplexed amplification schemes in future SDM systems.

We described a new measurement technique that employs a raster-scanned NSOM tip to accurately measure the spatiotemporal nonlinear dynamics within the duration of a single pulse—which reveals patterns that are not possible to observe using traditional CCD/CMOS cameras and optical spectrum analyzers. For the case of two LP<sub>0m</sub> modes excited in a step-index FMF, our measurements uncover a time-dependent mode interference effect arising from nonlinear interaction between the two modes. Specifically, we demonstrate the existence of interference fringes in the time-domain output, as predicted by the GMM-NLSE. Further, upon reconstruction using the raster-scanned measurements, we see that the instantaneous intensity profile at the FMF output end-face undergoes a time-dependent transformation. These form the first complete spatiotemporal measurements of multimode nonlinearity, to our knowledge.

The modal nature of multimode nonlinearity is confirmed through numerical simulations, which match the observations. The results are also consistent with observations obtained by thermal tuning, confirming that the observed effects are caused by mode interference.

The effects of optical nonlinearity in MMFs are fundamentally spatiotemporal in nature. To best understand the physics of these systems and the nonlinear dynamics that arise in them, a full (2 + 1)D diagnostic that can measure in both space and time (or frequency) is required [37]. The near-field measurement technique that we presented here serves as a promising tool with which to better understand nonlinear optics in MMFs and FMFs.

**Acknowledgment.** We acknowledge the support of the Maryland NanoCenter and its AIMLab.

**Disclosures.** The authors declare no conflicts of interest.

## REFERENCES

1. P. Mitra and J. Stark, “Nonlinear limits to the information capacity of optical fibre communications,” *Nature* **411**, 1027–1030 (2001).
2. R. Essiambre, G. Kramer, P. J. Winzer, G. J. Foschini, and B. Goebel, “Capacity limits of optical fiber networks,” *J. Lightwave Technol.* **28**, 662–701 (2010).
3. D. J. Richardson, J. M. Fini, and L. E. Nelson, “Space-division multiplexing in optical fibres,” *Nat. Photonics* **7**, 354–362 (2013).
4. N. Bai, E. Ip, Y.-K. Huang, E. Mateo, F. Yaman, M.-J. Li, S. Bickham, S. Ten, J. L. Nares, C. Montero, V. Moreno, X. Prieto, V. Tse, K. M. Chung, A. P. T. Lau, H.-Y. Tam, C. Lu, Y. Luo, G.-D. Peng, G. Li, and T. Wang, “Mode-division multiplexed transmission with inline few-mode fiber amplifier,” *Opt. Express* **20**, 2668–2680 (2012).
5. R.-J. Essiambre, R. Tkach, and R. Ryf, *Fiber Nonlinearity and Capacity: Single-Mode and Multimode Fibers* (Elsevier, 2013), pp. 1–43.
6. Z. Liu, L. G. Wright, D. N. Christodoulides, and F. W. Wise, “Kerr self-cleaning of femtosecond-pulsed beams in graded-index multimode fiber,” *Opt. Lett.* **41**, 3675–3678 (2016).
7. K. Krupa, A. Tonello, B. M. Shalaby, M. Fabert, A. Barthélémy, G. Millot, S. Wabnitz, and V. Couderc, “Spatial beam self-cleaning in multimode fibres,” *Nat. Photonics* **11**, 237–241 (2017).
8. W. H. Renninger and F. W. Wise, “Optical solitons in graded-index multimode fibres,” *Nat. Commun.* **4**, 1719 (2013).
9. K. Krupa, A. Tonello, A. Barthélémy, V. Couderc, B. M. Shalaby, A. Bendahmane, G. Millot, and S. Wabnitz, “Observation of geometric parametric instability induced by the periodic spatial self-imaging of multimode waves,” *Phys. Rev. Lett.* **116**, 183901 (2016).
10. M. A. Eftekhar, L. G. Wright, M. S. Mills, M. Kolesik, R. A. Correa, F. W. Wise, and D. N. Christodoulides, “Versatile supercontinuum generation in parabolic multimode optical fibers,” *Opt. Express* **25**, 9078–9087 (2017).
11. L. G. Wright, Z. Liu, D. A. Nolan, M.-J. Li, D. N. Christodoulides, and F. W. Wise, “Self-organized instability in graded-index multimode fibres,” *Nat. Photonics* **10**, 771–776 (2016).
12. A. Picozzi, G. Millot, and S. Wabnitz, “Nonlinear virtues of multimode fibre,” *Nat. Photonics* **9**, 289–291 (2015).
13. J. W. Nicholson, A. D. Yablon, S. Ramachandran, and S. Ghalmi, “Spatially and spectrally resolved imaging of modal content in large-mode-area fibers,” *Opt. Express* **16**, 7233–7243 (2008).
14. P. Bowlan, P. Gabolde, A. Shreenath, K. McGresham, R. Trebino, and S. Akturk, “Crossed-beam spectral interferometry: a simple, high-spectral-resolution method for completely characterizing complex ultrashort pulses in real time,” *Opt. Express* **14**, 11892–11900 (2006).
15. G. Pariente, V. Gallet, A. Borot, O. Gobert, and F. Quéré, “Space-time characterization of ultra-intense femtosecond laser beams,” *Nat. Photonics* **10**, 547–553 (2016).
16. Z. Guang, M. Rhodes, and R. Trebino, “Measuring spatiotemporal ultrafast field structures of pulses from multimode optical fibers,” *Appl. Opt.* **56**, 3319–3324 (2017).
17. P. Gabolde and R. Trebino, “Single-frame measurement of the complete spatiotemporal intensity and phase of ultrashort laser pulses using wavelength-multiplexed digital holography,” *J. Opt. Soc. Am. B* **25**, A25–A33 (2008).
18. K. Krupa, A. Tonello, V. Couderc, A. Barthélémy, G. Millot, D. Modotto, and S. Wabnitz, “Spatiotemporal light-beam compression from nonlinear mode coupling,” *Phys. Rev. A* **97**, 043836 (2018).
19. K. Krupa, C. Louot, V. Couderc, M. Fabert, R. Guenard, B. M. Shalaby, A. Tonello, D. Pagnoux, P. Leproux, A. Bendahmane, R. Dupiol, G. Millot, and S. Wabnitz, “Spatiotemporal characterization of supercontinuum extending from the visible to the mid-infrared in a multimode graded-index optical fiber,” *Opt. Lett.* **41**, 5785–5788 (2016).
20. J. C. Jing, X. Wei, and L. V. Wang, “Spatio-temporal-spectral imaging of non-repeatable dissipative soliton dynamics,” *Nat. Commun.* **11**, 2059 (2020).
21. Y. Leventoux, G. Granger, A. Tonello, S. Wabnitz, K. Krupa, G. Millot, S. Février, and V. Couderc, “Spatio-temporal beam mapping for studying nonlinear dynamics in graded index multimode fiber,” in *Conference on Lasers and Electro-Optics* (Optical Society of America, 2020), paper SM4P.4.
22. Y. Leventoux, G. Granger, K. Krupa, A. Tonello, G. Millot, M. Ferraro, F. Mangini, M. Zitelli, S. Wabnitz, S. Février, and V. Couderc, “3D time-domain beam mapping for studying nonlinear dynamics in multimode optical fibers,” arXiv:2010.02159v1 (2020).
23. F. Poletti and P. Horak, “Description of ultrashort pulse propagation in multimode optical fibers,” *J. Opt. Soc. Am. B* **25**, 1645–1654 (2008).
24. L. Rishøj, B. Tai, P. Kristensen, and S. Ramachandran, “Soliton self-mode conversion: revisiting Raman scattering of ultrashort pulses,” *Optica* **6**, 304–308 (2019).
25. Z. Zhu, L. G. Wright, J. Carpenter, D. Nolan, M.-J. Li, D. N. Christodoulides, and F. W. Wise, “Mode-resolved control and measurement of nonlinear pulse propagation in multimode fibers,” in *Conference on Lasers and Electro-Optics* (Optical Society of America, 2018), paper FTh4E.7.
26. Z. Xie, S. Gao, T. Lei, S. Feng, Y. Zhang, F. Li, J. Zhang, Z. Li, and X. Yuan, “Integrated (de)multiplexer for orbital angular momentum fiber communication,” *Photon. Res.* **6**, 743–749 (2018).
27. C.-L. Chen, “Excitation of higher order modes in optical fibers with parabolic index profile,” *Appl. Opt.* **27**, 2353–2356 (1988).
28. F. Schiappelli, R. Kumar, M. Prascioli, D. Cojoc, S. Cabrini, M. De Vittorio, G. Visimberga, A. Gerardino, V. Degiorgio, and E. Di Fabrizio,

- "Efficient fiber-to-waveguide coupling by a lens on the end of the optical fiber fabricated by focused ion beam milling," *Microelectron. Eng.* **73-74**, 397–404 (2004), Micro and Nano Engineering 2003.
29. T. Gissibl, M. Schmid, and H. Giessen, "Spatial beam intensity shaping using phase masks on single-mode optical fibers fabricated by femtosecond direct laser writing," *Optica* **3**, 448–451 (2016).
30. K. Weber, F. Hütt, S. Thiele, T. Gissibl, A. Herkommer, and H. Giessen, "Single mode fiber based delivery of OAM light by 3D direct laser writing," *Opt. Express* **25**, 19672–19679 (2017).
31. A. M. Konzelmann, S. O. Krüger, and H. Giessen, "Interaction of orbital angular momentum light with Rydberg excitons: modifying dipole selection rules," *Phys. Rev. B* **100**, 115308 (2019).
32. G. Kostovski, P. R. Stoddart, and A. Mitchell, "The optical fiber tip: an inherently light-coupled microscopic platform for micro- and nanotechnologies," *Adv. Mater.* **26**, 3798–3820 (2014).
33. K. Ho and J. M. Kahn, "Linear propagation effects in mode-division multiplexing systems," *J. Lightwave Technol.* **32**, 614–628 (2014).
34. S. Ramachandran, P. Kristensen, and M. F. Yan, "Generation and propagation of radially polarized beams in optical fibers," *Opt. Lett.* **34**, 2525–2527 (2009).
35. S. Ramachandran and P. Kristensen, "Optical vortices in fiber," *Nanophotonics* **2**, 455–474 (2013).
36. P. Horak and F. Poletti, *Multimode Nonlinear Fibre Optics: Theory and Applications* (IntechOpen, 2012), pp. 1–24, Chap. 1.
37. K. Krupa, A. Tonello, A. Barthélémy, T. Mansuryan, V. Couderc, G. Millot, P. Grelu, D. Modotto, S. A. Babin, and S. Wabnitz, "Multimode nonlinear fiber optics, a spatiotemporal avenue," *APL Photon.* **4**, 110901 (2019).